Biomimetic Intelligence and Robotics 4 (2024) 100191

Contents lists available at ScienceDirect

Biomimetic Intelligence and Robotics

journal homepage: www.elsevier.com/locate/birob

Research Article

Design and kinematics analysis of a cable-stayed notch manipulator for transluminal endoscopic surgery

Yanqiang Lei [a,b,c], Fuxin Du [b], Huajian Song [a], Liping Zhang [d,*]

[a] School of Automation and Electrical Engineering, Linyi University, Linyi 276000, China
[b] School of Mechanical Engineering, Shandong University, Jinan 250061, China
[c] MH Robot & Automation Co., LTD., Zhucheng 262100, China
[d] School of Logistics, Linyi University, Linyi 276000, China

ARTICLE INFO

Article history:
Received 26 July 2024
Revised 29 September 2024
Accepted 21 October 2024
Available online 28 October 2024

Keywords:
Medical robot
Comprehensive elliptic integral solution
Kinematics
Notch continuum manipulator
Transluminal endoscopic surgery

ABSTRACT

The friction between the joints of the continuum manipulator with discrete joints brings great difficulties to kinematic modeling. The traditional driving wire arrangement limits the load capacity of the manipulator. A cable-stayed notch manipulator for transluminal endoscopic surgery is proposed, and a driving force coupling kinematic mode is established. The manipulator is fabricated from a superelastic Nitinol tube with bilaterally cut rectangular notches and is actuated by a stay cable. By applying the comprehensive elliptic integral solution (CEIS) for large deformation beams, the bending angle of each elastic beam is obtained, and the kinematics from the driving space to the joint space is formed. According to the bending angle of each elastic beam, the expression of the manipulator in Cartesian space can be obtained by geometric analysis. The kinematics from the joint space to the Cartesian space is established. The outer diameter of the manipulator is only 3.5 mm, and the inner diameter can reach 2 mm, allowing instruments to pass through. The maximum error of the manipulator movement is less than 5%. The load capacity of the manipulator has been verified through the stiffness experiments, and the maximum load of the manipulator can reach 400 g. The cable-stayed notch manipulator can be accurately modeled on the base of CEIS, and its motion accuracy can meet the needs of engineering applications. The compact size and excellent load capacity of the manipulator make it potential for application in transluminal endoscopic surgical robots.

1. Introduction

Transluminal endoscopic surgery has become the first choice for the treatment of early gastrointestinal tumors [1]. The doctor inserts the endoscope into the human body through the patient's mouth or anus. The doctor controls the flexible part of the endoscope by operating the handwheel, which can perform simple operations such as marking, injection, and stripping [2]. When using a traditional endoscope to perform endoscopic mucosal dissection (ESD), due to the poor flexibility of the instrument and the influence of gravity, the submucosal incision field of view is obstructed, which may easily lead to bleeding or perforation [3]. To improve the safety of surgery, and broaden the surgical methods of endoscopic surgery, developing more flexible manipulators has become a hot research issue [4]. Continuum manipulators are widely used in the development of endoscopic surgical manipulators due to their lightweight, small size, and good applicability in narrow environments.

The continuum manipulator has a variety of driving methods, but the gas-driven manipulator [5] and the motor-driven manipulator [6] are difficult to miniaturize. The continuum manipulators used in minimally invasive surgical robots are mostly wire-driven or rod-driven [7]. A manipulator using a dual continuum mechanism was proposed by Xu et al. for laparoscopic surgical robots [8]. The manipulator is driven by multiple elastic rods, which have good flexibility and strong load capacity. The manipulator is designed for laparoscopic surgical robots, and there are many challenges in reducing the diameter. The manipulator in the Single-Port Surgery (SPS) system is assembled by links and hinges [9]. The linkage mechanism has excellent load capacity. If the manipulator is designed to pass through the narrow instrument channel of the endoscope, the processing of the links and hinges will be very difficult. Therefore, it is difficult to miniaturize the manipulator with a complex structure, which cannot meet the size requirements of the endoscopic surgical robot.

A tendon-sheath transmission mechanism and an articulated manipulator are used in the "MASTER" system [10]. The manipulator has five degrees of freedom (DoFs), which can meet the

* Corresponding author.
E-mail address: zhangliping@lyu.edu.cn (L. Zhang).

https://doi.org/10.1016/j.birob.2024.100191

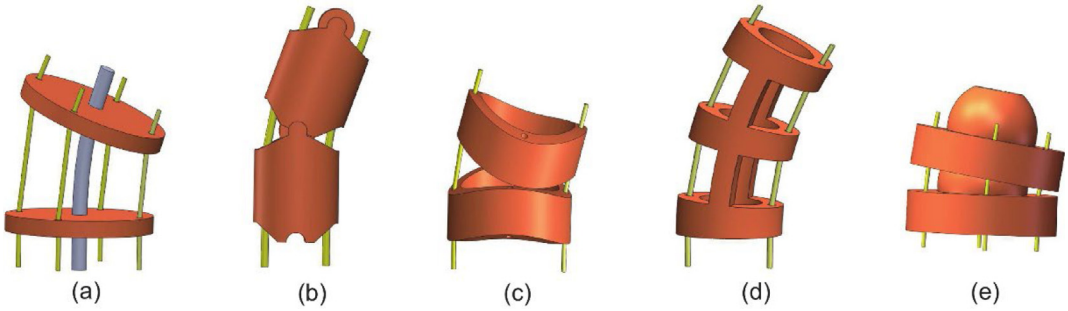

Fig. 1. Joint structure of continuum manipulator. (a) Disc joints. (b) Hinge joint. (c) Rolling joint. (d) Notched tube joint. (e) Spherical joint.

flexibility requirements of transluminal endoscopic treatment. The system does not utilize the instrument channel of the endoscope. The manipulators are attached to the end of the endoscope, which may interfere with intraoperative instrument change and sterilization of surgical instruments. Based on the general endoscopic platform of USGI, a surgical robotic system for transluminal endoscopic surgery was developed by Lau et al. [11], and the joint structure is shown in Fig. 1(a). A continuum manipulator for laparoscopic surgery using hinge joints was developed by Wang et al. [12], as shown in Fig. 1(b). The "Viacath" system is designed for transluminal endoscopic surgery [13], which also uses hinge joints. The diameter of the manipulator is only 7.2 mm. To increase the load capacity, a continuum manipulator with rolling joints was developed by Suh et al. [14], and the joint structure is shown in Fig. 1(c). A continuum manipulator for bone drilling under a curved approach was developed by Alambeigi et al. [15]. The joint structure is shown in Fig. 1(d). The manipulator is machined from a Nitinol tube with a rectangular cut. As shown in Fig. 1(e), a spherical joint continuum manipulator was developed by Lu et al. and an efficient inverse kinematics algorithm was designed [16,17]. The manipulator has poor torsional stiffness. As Fig. 1 shows, the above joint structures have the same characteristics. The driving wire passes through the sidewall of each joint in turn, and the tension of the driving wire between adjacent joints determines the maximum load capacity of the manipulator. To obtain higher manipulator load capacity while meeting the diameter constraints of transluminal endoscopic surgery, Hwang et al. proposed a strong continuum manipulator [18]. However, the manipulator still uses hinge joints, and the friction analysis between joints cannot be avoided.

Among the traditional drive wire arrangements, the rolling joint has the best load capacity compared to other joint forms. The load capacity of the manipulator can be further increased by using a stay cable. The manipulator of the hinged joint has better torsional stiffness than the guided disc joint [19]. However, due to the uneven distribution of friction between adjacent joints in the manipulator of the hinge joint or rolling joint, it is difficult to accurately model the friction of each joint under underactuated conditions [20]. To overcome this problem, Li et al. developed a continuum manipulator with each joint independently driven [21]. However, it is challenging to deploy a complex tendon-sheath mechanism within the limited size of the manipulator. The notched tube joint does not need to consider the friction between joints, which provides convenience for modeling and has better torsional stiffness [22]. Du et al. designed a notched tube manipulator [23,24], using Timoshenko beam theory to model the manipulator, which has higher modeling accuracy than the piecewise constant curvature assumption, but the manipulator has only one DoF. Zhang et al. designed a compound continuum manipulator for minimally invasive surgery [25], the manipulator combines the concentric tube structure with the notched tube structure to improve the load capacity. Wang et al. designed a manipulator for throat surgery [26,27], and the small deformation cantilever beam theory was used to establish the kinematics. However, the manipulator uses a double-layer structure, making it difficult to miniaturize.

According to the comprehensive analysis of the above literature, the manipulator used for transluminal endoscopic surgery needs to satisfy the following requirements [28,29]: (1) The diameter of the manipulator should be small enough to pass through the instrument channel of the endoscope. (2) The manipulator should have sufficient load capacity and dexterity to complete surgical operations such as lifting and cutting. (3) The manipulator should have a simple mechanism and can carry out accurate modeling for control. To meet the needs of transluminal endoscopic surgery, this paper proposed a cable-stayed notch manipulator. The main contributions of this paper can be summarized as follows:

◆ A continuum manipulator that can be accurately modeled and has a large load capacity is proposed. The manipulator is machined with a Nitinol tube cut, which has better torsional stiffness than the disc joint. The elastic beam of the notched tube replaces the hinge joint or the spherical joint, which avoids the friction analysis between the joints and lays the foundation for the accurate kinematic modeling of the manipulator. The stay cable is used to drive the manipulator, which enhances the load capacity of the manipulator.

◆ A driving force coupling kinematic model of the manipulator is established based on the CEIS. Based on the force applied by the stay cable to the manipulator, the transmission of forces and moments on the manipulator is analyzed. Using the CEIS, the bending angles of elastic beams under force and moment are obtained. The kinematics from driving space to joint space is formed. According to the bending angle of each elastic beam, the geometric analysis method is applied to further obtain the position of the manipulator. The kinematics from joint space to the Cartesian spaces is formed.

◆ A prototype was built to verify the kinematic model and load capacity of the manipulator. The kinematics verification experiment shows that the maximum error of the manipulator movement is less than 5%, which can meet the requirements of engineering applications. The load capacity experiment shows that the maximum load of the manipulator can reach 400 g.

2. Materials and methods

2.1. Design description

As shown in Fig. 2(a), the outer diameter of the continuum manipulator for endoscopic surgery proposed in this paper is only 3.5 mm in outer diameter and 28 mm in length. The inside of the manipulator is a hollow structure with a diameter of 2 mm, which

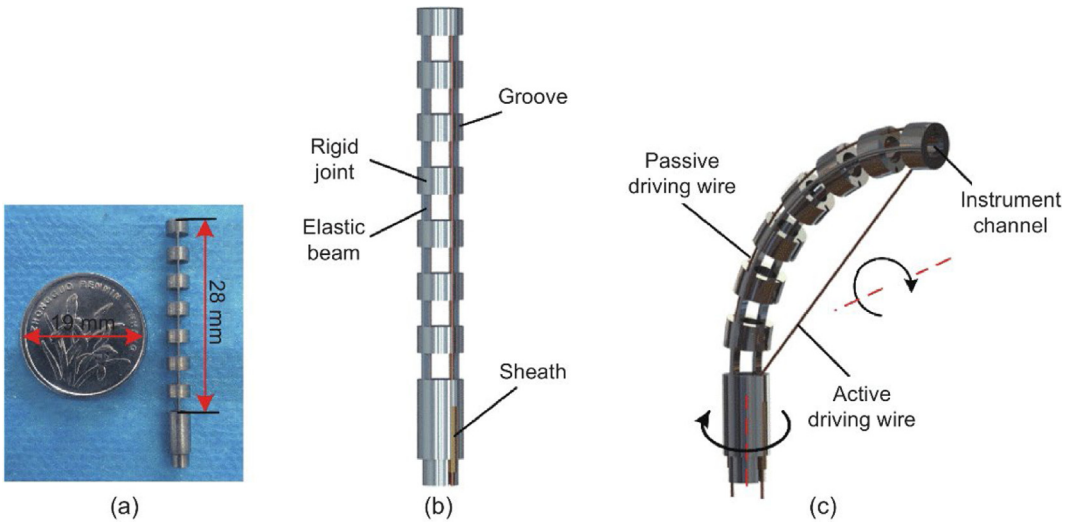

Fig. 2. Model and prototype of the continuum manipulator. (a) Manipulator size, (b) Unbent state of the continuum manipulator, (c) Bending state of the continuum manipulator.

can allow the passage of surgical instruments such as clamps and electric knives.

As shown in Fig. 2(b), The manipulator contains two DoFs, bending and rotation. The manipulator is driven by a pair of antagonistic driving wires, one end of the driving wire is fixed at the end joint of the manipulator, and the other end of the driving wire is connected to the driving mechanism through the hole of the base joint. The active driving wire overcomes the elastic force of the elastic beam to bend the manipulator. After the active driving wire is slackened, the manipulator cannot fully return to its initial position, and the passive driving wire is used to correct the manipulator. The diameter of the hole on the end joint and the base joint of the manipulator is 0.5 mm, and the diameter of the driving wire is 0.3 mm. As shown in Fig. 1(b), there are grooves on both sides of the manipulator on the axis of the driving wire hole. When the manipulator is not bent, the driving wire can be hidden in the groove, and the manipulator can pass through the instrument channel of the endoscope. When the manipulator is bent, the active driving wire is released from the groove to form a cable-stayed mechanism. The cable-stayed mechanism can significantly improve the load capacity of the manipulator.

Nitinol is widely used in the processing of medical devices due to its good biocompatibility and superelasticity [30]. The cable-stayed notch manipulator is also made of Nitinol. Square grooves are cut on the Nitinol tube by an Electrical Discharge Machining (EDM), and the manipulator is divided into two parts: a rigid joint and an elastic beam. The depth of the square cut is 1.6 mm, and the depth of the square cut determines the stiffness of the elastic beam. To facilitate the processing of the manipulator, the height of the rigid joint and the elastic beam are both 2 mm. Driving wire grooves and holes are machined by EDM drilling. The width of the grooves is 0.5 mm and the depth of the grooves is 0.38 mm. Compared with the previous notch continuum manipulator, the machining of grooves is easier than the machining of fine and deep holes [31].

2.2. Kinematic analysis of a cable-stayed notch manipulator

The manipulator is divided into rigid joints and elastic beams, and the bending of the manipulator is realized by the cumulative bending of the elastic beam. The bending of the elastic beam is caused by the force and moment on the end of the manipulator, so the kinematics and mechanical models of the manipulator are coupled. In this chapter, the bending angle of the elastic beam is obtained by analyzing the transmission of force and moment, and the kinematics from the driving space to the joint space is formed. According to the bending angle of each elastic beam, the geometric analysis is applied to establish the kinematics from joint space to Cartesian space. Finally, the complete kinematics is established.

Compared with the traditional driving wire arrangement, the driving wire of the cable-stayed manipulator only exerts the pulling force on the end joint of the manipulator. The bending of the elastic beam is achieved by the force and moment transmitted from the end of the manipulator. The driving wire has no contact with the middle joint of the manipulator, and the relative sliding only exists between the driving wire and the hole of the base joint, which simplifies the friction analysis of the manipulator. Therefore, the controller of the continuum manipulator can be established by the mechanical model.

To realize the kinematic modeling of the cable-stayed notch manipulator, reasonable assumptions need to be made for the manipulator:

(1) When the manipulator is bent, the length of the elastic beam does not change, only bending deformation occurs. The bending of the elastic beam can be regarded as a constant curvature, and the rigid joint does not deform.

(2) When the manipulator is bent, the passive driving wire does not generate friction and driving force on the manipulator.

(3) The bending stiffness of the driving wire is not considered when the manipulator is bent. The gap between the active driving wire and the threading hole is negligible.

(4) A quasi-static equilibrium state can be achieved under the action of friction, and the friction is equal to the maximum static friction.

2.2.1. The deflection of the elastic beam under force and moment

The bending angle of the elastic beam under force and moment is related to the stiffness of the elastic beam. The bending stiffness of an elastic beam can be expressed as $K=EI$, where E is the elastic modulus and I is the moment of inertia. E is the same everywhere in the homogeneous Nitinol tube. As shown in Fig. 3, a coordinate system is established to analyze the moment of inertia of the elastic beam. According to the bending direction of the elastic beam, the z-axis is the neutral axis of the moment of

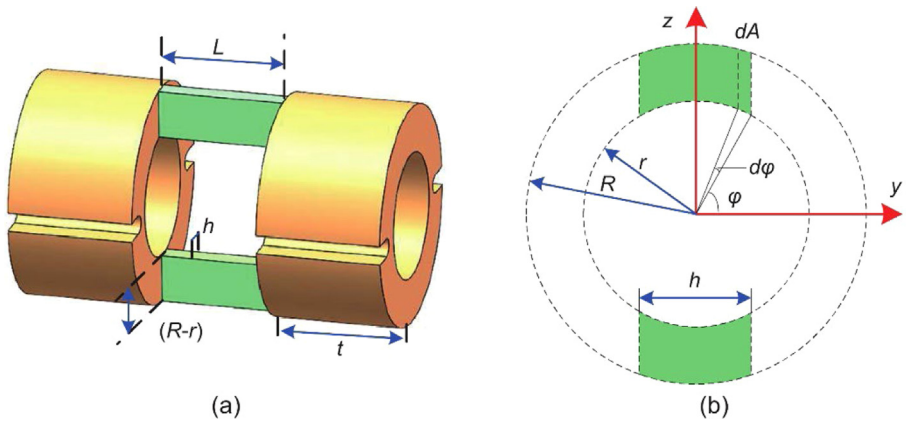

Fig. 3. Elastic beam of the notch manipulator. (a) Structural parameters of the elastic beam, (b) Moment of inertia of elastic beam.

inertia. From the definition of the moment of inertia, the moment of inertia of the elastic beam can be expressed as Eq. (1).

$$\begin{aligned} I_z &= \int y^2 dA \\ &= \int_{\arccos(h/2r)}^{\pi-\arccos(h/2r)} 2(r\cos\varphi)^2(\sqrt{R^2 - r^2\cos^2\varphi} - r\sin\varphi) r\sin\varphi d\varphi \\ &= 4\int_{\arccos(h/2r)}^{\pi/2} (r\cos\varphi)^2(\sqrt{R^2 - r^2\cos^2\varphi} - r\sin\varphi) r\sin\varphi d\varphi \end{aligned} \tag{1}$$

where A is the critical area of the element, and φ represents the angle between the microelement and the y-axis. As shown in Fig. 3(a), h is the thickness of the elastic beam, L is the length of the elastic beam. r is he inner radius and R is the outer radius of the manipulator.

To analyze the bending situation of the manipulator, the force analysis of a single elastic beam is carried out first. The elastic beam of the manipulator can be considered as a cantilever beam subjected to the combined action of force and moment. As shown in Fig. 4, $(x_{i\_b}, y_{i\_b}, z_{i\_b})$ and $(x_{i\_e}, y_{i\_e}, z_{i\_e})$ represent the base coordinate system and the end coordinate system of the ith elastic beam, respectively. F_i and M_i represent the force and moment applied at the end of the elastic beam. When the manipulator is bent, a_i and b_i are the coordinates in the x_{i_b} and y_{i_b} directions, respectively. α_i is the angle between F_i and x_{i_b}-axis. θ_i is the angle of the elastic beam after bending. According to the given forces and boundary conditions, the deflection problem of the elastic beam can be solved by the elliptic integration method [32]. The deflection of the elastic beam under the force F_i can be solved by Eq. (2).

$$\sqrt{\frac{F_i L^2}{EI_z}} = F(\pi/2, k) - F(\Theta, k) \tag{2}$$

where

$$\begin{cases} F(\gamma, k) = \int_0^{\gamma} \dfrac{d\theta}{\sqrt{1 - k^2\sin^2(\theta)}} \\ k = \sin\dfrac{\alpha_i + \theta_{Fi}}{2} \\ \Theta = asin(\sin(\alpha_i/2)/k) \end{cases} \tag{3}$$

where $F(\gamma, k)$ is the elliptic integral of the first kind, and Eq. (2) can be solved with the "fsolve" function in Matlab. θ_{Fi} is the deflection angle of the elastic beam under the action of the force F_i. Under the combined effort of force and moment, the deflection angle of the elastic beam can be expressed as Eq. (4).

$$\theta_i = \frac{M_i L}{EI} + \theta_{Fi} \tag{4}$$

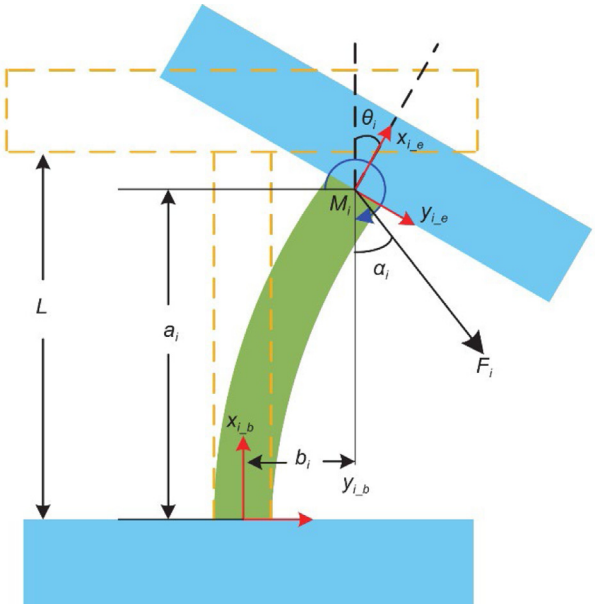

Fig. 4. Deformation analysis of elastic beam.

According to Assumption (1), the bending of the elastic beam can be regarded as an arc of constant curvature, and the deflection displacement of the elastic beam can be expressed by Eq. (5).

$$\begin{cases} a_i = L\sin(\theta_i)/\theta_i \\ b_i = L(1 - \cos(\theta_i))/\theta_i \end{cases} \tag{5}$$

2.2.2. The kinematics from driving space to joint space

To analyze the force of each elastic beam on the manipulator, the coordinate system shown in Fig. 5 is established. The manipulator has n elastic beams, the one near the base is defined as the first, and the elastic beam near the end of the manipulator is defined as the n-th one. A local coordinate system is established at both ends of each elastic beam, the coordinate system at the base of the elastic beam is defined as $(x_{i\_b}, y_{i\_b}, z_{i\_b})$ and the coordinate system at the end of the elastic beam is defined as $(x_{i\_e}, y_{i\_e}, z_{i\_e})$.

As shown in Fig. 5, a represents the action point of the driving wire on the manipulator, and b represents the point where the driving wire passes through the base of the manipulator. F_t represents the pulling force applied to the manipulator. F_p represents the pulling force of the driving wire, and the friction between the driving wire and base joint is equal to F_p - F_t. The force and

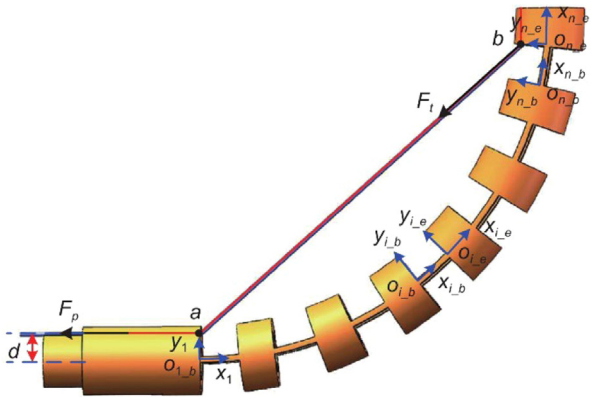

Fig. 5. Force analysis of elastic beams.

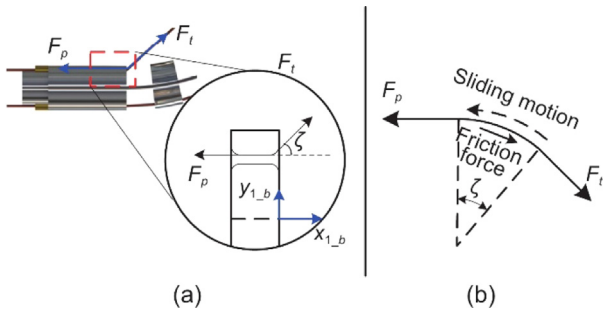

Fig. 6. Analysis of friction between the driving wire and joint.

moment applied to the n-th elastic beam can be expressed by Eq. (6).

$$\begin{cases} {}^{n\_b}\boldsymbol{F}_t = F_t\,{}^{n\_b}\boldsymbol{e}_{ba} \\ {}^{n\_b}\boldsymbol{M} = {}^{n\_b}\boldsymbol{F}_t \times {}^{n\_b}\boldsymbol{o}_{n\_e}\,{}^{n\_b}\boldsymbol{b} \end{cases} \tag{6}$$

Where ${}^{n\_b}\boldsymbol{F}_t$ represents the pulling force vector of the driving wire in the coordinate system $(x_{n\_b}, y_{n\_b}, z_{n\_b})$, ${}^{n\_b}\boldsymbol{e}_{ba}$ represents the unit vector of $\overrightarrow{ba}$ in the coordinate system $(x_{n\_b}, y_{n\_b}, z_{n\_b})$, ${}^{n\_b}\boldsymbol{b}$ illustrates the point b in the coordinate system $(x_{n\_b}, y_{n\_b}, z_{n\_b})$, and ${}^{n\_b}\boldsymbol{o}_{n\_e}$ represent the origin of coordinate system $(x_{n\_e}, y_{n\_e}, z_{n\_e}$)in the coordinate system$(x_{n_b}, y_{n_b}, z_{n_b})$. In the definition of the coordinate system, the letter "n" in the corner mark indicates the serial number of the elastic joint. A corner mark "n_b" represent the start point of the coordinate system defined at the elastic joint. Similarly, a corner mark "n_e" indicate that the coordinate system is defined at the end of an elastic joint. The upper left subscript of the symbol indicates the reference coordinate system, the other symbols in this paper have the same expression.

According to Assumption 1, the elastic beam can be considered an arc of constant curvature. The bending angle of the ith elastic beam is θ_i, then the homogeneous transformation matrix from $(x_{n\_e}, y_{n\_e}, z_{n\_e})$ to $(x_{n\_b}, y_{n\_b}, z_{n\_b})$ can be expressed as Eq. (7).

$${}^{n\_b}_{n\_e}\boldsymbol{T} = \begin{bmatrix} \cos\theta_n & -\sin\theta_n & 0 & a_n \\ \sin\theta_n & \cos\theta_n & 0 & b_n \\ 0 & 0 & 1 & 0 \\ 0 & 0 & 0 & 1 \end{bmatrix} \tag{7}$$

The distance from the driving wire hole to the axis of the manipulator is d. Point b and ${}^{n\_e}o_{org}$ can be easily obtained by geometric analysis.

$$\begin{cases} {}^{n\_e}\boldsymbol{b} = \begin{bmatrix} 0 & d & 0 \end{bmatrix} \\ {}^{n\_e}\boldsymbol{o}_{org} = \begin{bmatrix} 0 & 0 & 0 \end{bmatrix} \end{cases} \tag{8}$$

Then the point ${}^{n\_b}b$ and ${}^{n\_b}o_{n\_e}$ can be expressed as Eq. (9)

$$\begin{cases} {}^{n\_b}\boldsymbol{b} = {}^{n\_b}_{n\_e}\boldsymbol{T}\,{}^{n\_e}\boldsymbol{b} \\ {}^{n\_b}\boldsymbol{o}_{n\_e} = {}^{n\_b}_{n\_e}\boldsymbol{T}\,{}^{n\_e}\boldsymbol{o}_{org} \end{cases} \tag{9}$$

The rigid joints of the manipulator cannot bend and compress and can be regarded as extensions along the tangential direction of the elastic beam. Starting from the coordinate system $(x_{1\_b}, y_{1\_b}, z_{1\_b})$, the adjacent elastic beams and rigid joints are regarded as a unit. Through geometric analysis, The homogeneous transformation matrix from $(x_{i\_b}, y_{i\_b}, z_{i\_b})$ to $(x_{i+1\_b}, y_{i+1\_b}, z_{i+1\_b})$ can be expressed as Eq. (10).

$${}^{i+1\_b}_{i\_b}\boldsymbol{T} = \begin{bmatrix} \cos\theta_i & \sin\theta_i & 0 & -(a_i + t\cos\theta_i) \\ -\sin\theta_i & \cos\theta_i & 0 & -(b_i + t\sin\theta_i) \\ 0 & 0 & 1 & 0 \\ 0 & 0 & 0 & 1 \end{bmatrix} \tag{10}$$

The vector ${}^{1\_b}\boldsymbol{a}$ can be obtained by geometric analysis, and the expression of the vector ${}^{n\_b}\boldsymbol{a}$ can be obtained by Eq. (11)

$${}^{n\_b}\boldsymbol{a} = {}^{n\_b}_{n-1\_b}\boldsymbol{T} \cdots {}^{3\_b}_{2\_b}\boldsymbol{T}\,{}^{2\_b}_{1\_b}\boldsymbol{T}\,{}^{1\_b}\boldsymbol{a} \tag{11}$$

Using the positions of point ${}^{n\_b}\boldsymbol{a}$ and point ${}^{n\_b}\boldsymbol{b}$, the unit vector ${}^{n\_b}\boldsymbol{e}_{ba}$ in the coordinate system $(x_{n\_b}, y_{n\_b}, z_{n\_b})$ can be expressed as Eq. (12).

$${}^{n\_b}\boldsymbol{e}_{ba} = \frac{{}^{n\_b}\boldsymbol{a} - {}^{n\_b}\boldsymbol{b}}{\left|{}^{n\_b}\boldsymbol{a} - {}^{n\_b}\boldsymbol{b}\right|} \tag{12}$$

So far, the complete expression of Eq. (6) has been obtained.

The forces and moments applied to the elastic beam in the middle of the manipulator have similar expressions. The force and moment applied to the ith elastic beam can be expressed as Eq. (13).

$$\begin{cases} {}^{i\_b}\boldsymbol{F}_t = F_t\,{}^{i\_b}\boldsymbol{e}_{ba} \\ {}^{i\_b}M = {}^{i\_b}\boldsymbol{F}_t \times {}^{i\_b}\boldsymbol{o}_{i\_e}\,{}^{i\_b}\boldsymbol{b} \end{cases} \tag{13}$$

The expression of ${}^{i\_b}\boldsymbol{a}$, ${}^{i\_b}\boldsymbol{b}$ and ${}^{n\_e}\boldsymbol{o}_{org}$ in the base coordinate system of the ith elastic beam can be obtained by Eq. (14).

$$\begin{cases} {}^{i\_b}\boldsymbol{a} = {}^{i\_b}_{i-1\_b}\boldsymbol{T} \cdots {}^{2\_b}_{1\_b}\boldsymbol{T}\,{}^{1\_b}\boldsymbol{b} \\ {}^{i\_b}\boldsymbol{b} = {}^{i\_b}_{i+1\_b}\boldsymbol{T} \cdots {}^{n-1\_b}_{n\_b}\boldsymbol{T}\,{}^{n\_b}\boldsymbol{b} \\ {}^{i\_b}\boldsymbol{o}_{i\_e} = {}^{i\_b}_{i\_e}\boldsymbol{T}\,{}^{i\_e}\boldsymbol{o}_{org} \end{cases} \tag{14}$$

Where ${}^{i\_b}_{i+1\_b}\boldsymbol{T}$ represent the homogeneous transformation matrix from $(x_{i+1\_b}, y_{i+1\_b}, z_{i+1\_b})$ to $(x_{i\_b}, y_{i\_b}, z_{i\_b})$, and the ${}^{i\_b}_{i+1\_b}\boldsymbol{T}$ can be expressed as Eq. (15)

$${}^{i\_b}_{i+1\_b}\boldsymbol{T} = \begin{bmatrix} \cos\theta_i & -\sin\theta_i & 0 & (a_i + t\cos\theta_i) \\ \sin\theta_i & \cos\theta_i & 0 & (b_i + t\sin\theta_i) \\ 0 & 0 & 1 & 0 \\ 0 & 0 & 0 & 1 \end{bmatrix} \tag{15}$$

As shown in Fig. 6, The driving wire and the base joint can be regarded as entanglement, and the friction between them can be described by the belt friction model [33]. The relationship between the input force of the driving wire F_p and the pulling force applied on the manipulator F_t can be expressed by Eq. (16).

$$F_t = F_p e^{-\mu\zeta} \tag{16}$$

where μ is the friction coefficient between the driving wire and the base joint, and ζ represents the angle between the force

applied on the manipulator F_t and x_{1_b}-axis. The angle ζ can be expressed by Eq. (17).

$$\zeta = \cos^{-1}({}^{1\_b}\boldsymbol{e}_x \cdot \frac{{}^{1\_b}\boldsymbol{a}\,{}^{1\_b}\boldsymbol{b}}{\left|{}^{1-b}\boldsymbol{a}\,{}^{1\_b}\boldsymbol{b}\right|}) \tag{17}$$

Where ${}^{1\_b}\boldsymbol{e}_x$ is the unit vector on x_{1_b} axis.

The bending angle of the elastic beam can be solved by the numerical iterative method. As shown in Fig. 7, the design parameters of the notch manipulator and the pulling force are already given. Before the iterative process starts, the initial bending angle of the elastic beam needs to be given first. Substituting the given initial bending angle and deflection distance into Eq. (7) to Eqs. (11) and (14), the corresponding transformation matrix and vector can be obtained. Further, according to Eqs. (6) and (13), the force and moment applied to each elastic beam of the manipulator can be obtained. The new bending angle and deflection displacement of the elastic beam can be obtained using Eq. (4). Judging whether the bending angle of the elastic beam has converged by comparing the new bending angle with the last bending angle. The iteration stops if the bending angle already meets the accuracy requirements. Otherwise, the iteration continues with the new bending angle. Although the calculation process of the method proposed in this paper has been illustrated in Fig. 7. A more detailed calculation process is given by Algorithm (1).

Algorithm 1: Manipulator bending angle solver

Initialize the parameters: manipulator mechanical parameters
Initialize the parameters: F_p, Maxgen, err /* Maxgen: Max iteration; err: Fitness err*/
Initialize the parameters: a_i, b_i, θ_i /* Initial state of manipulator*/
for t = 1: Maxgen **do** /*iteration number: t*/
  Calculate F_t using Eq. (16) and Eq. (17)
  Calculate ${}^{i\_b}\boldsymbol{a}$, ${}^{i\_b}\boldsymbol{b}$ using Eq. (14)
  Calculate ${}^{i\_b}_{i+1\_b}\boldsymbol{T}$, ${}^{i+1\_b}_{i\_b}\boldsymbol{T}$ using Eq. (10) and Eq. (15)
  Calculate ${}^{i\_b}M$, ${}^{i\_b}\boldsymbol{F}$ using Eq. (13)
  Update the bending angle of elastic beam using Eq. (4) of ${}^{new}\theta_i$
  Update the deflection distance using Eq. (5) of ${}^{new}a_i$, ${}^{new}b_i$
  Calculate err = ${}^{new}\theta_i - \theta_i$
  if err < $1e-03$ **then**
    Bending angle of elastic beam $\theta_i = {}^{new}\theta_i$
    deflection distance $a_i = {}^{new}a_i$, $b_i = {}^{new}b_i$
    break
  else
    Bending angle of elastic beam $\theta_i = {}^{new}\theta_i$
    deflection distance $a_i = {}^{new}a_i$, $b_i = {}^{new}b_i$
    iteration number $t = t + 1$
  end if
end for

2.2.3. The kinematics from joint space to cartesian space

Unlike traditional rigid link robots, it is difficult to describe the motion of the notch manipulator proposed in this paper using only link lengths and joint angles. As shown in Fig. 8, the Cartesian coordinate system is established at the base of the manipulator. Considering the overall rotation of the manipulator, the coordinate transformation from the base coordinate system of the manipulator to the Cartesian fixed coordinate system can be achieved by the following process: (1) The manipulator rotates angle Φ counterclockwise around the x_1- axis, (2) The manipulator rotates the angle $\pi/2$ counterclockwise around the y_1- axis. The coordinate transformation matrix can be expressed as Eq. (18)

$${}^0_1\boldsymbol{T} = \begin{bmatrix} 0 & \sin\Phi & \cos\Phi & 0 \\ 0 & \cos\Phi & -\sin\Phi & 0 \\ -1 & 0 & 0 & 0 \\ 0 & 0 & 0 & 1 \end{bmatrix} \tag{18}$$

The combination of elastic beam and rigid joint can be regarded as a unit. When the elastic beam is bent, the link moves along the y_i- axis for a distance $L(1\text{-}cos(\theta_i))/\,\theta_i + tsin(\theta_i)$, along the x_i- axis for a distance $Lsin(\theta_i)/\,\theta_i + tcos(\theta_i)$. θ_i is the bending angle, which has been obtained by numerical iteration.

$${}^i_{i+1}\boldsymbol{T} = \begin{bmatrix} \cos\theta_i & -\sin\theta_i & 0 & L\sin(\theta_i)/\theta_i + t\cos\theta_i \\ \sin\theta_i & \cos\theta_i & 0 & L(1-\cos(\theta_i))/\theta_i + t\sin\theta_i \\ 0 & 0 & 1 & 0 \\ 0 & 0 & 0 & 1 \end{bmatrix}, i \geq 1 \tag{19}$$

The kinematics of the manipulator from joint space to Cartesian space can be expressed as Eq. (20)

$${}^0_nT = {}^0_1T\,{}^1_2T\,{}^2_3T \cdots {}^i_{i+1}T \cdots {}^{n-2}_{n-1}T\,{}^{n-1}_nT \tag{20}$$

2.3. Prototype and experimental verification

The control accuracy and load capacity of the manipulator are the keys to endoscopic surgery and are also the main difficulties in the development of miniature manipulators. In this paper, the kinematics from driving space to joint space and the kinematics from joint space to Cartesian space are respectively verified by two experiments. Finally, the load capacity of the manipulator is proved by the weightlifting experiment.

2.3.1. Experiment of elastic beam bending

According to the method proposed in this paper, the bending angle of the elastic beam can be obtained by numerical iteration with the driving force. To verify the effectiveness of the method, an experimental setup as shown in Fig. 9 was established. The continuum manipulator was fixed to the bench by a 3D-printed bracket. The driving wire of the continuum manipulator was connected to the weight around the guide wheel. The camera (MV-CE100-30GM, Hikvision, China, distinguishability: 3840 × 2748) perpendicular to the motion plane of the manipulator was used to capture the bending of the elastic beam.

The actual bending angle of the elastic beam was obtained from the image captured by the camera. The reference bending angle of the elastic beam was calculated by simulation. All calculations were performed on a computer equipped with an Intel Core i7 CPU at 3.9 GHz and 16 GB of RAM. The initial conditions and design parameters of the manipulator are summarized in Table 1.

2.4. Manipulator kinematic model validation

To verify the kinematics of the manipulator from the driving space to the working space, the experimental setup shown in Fig. 10 was built. The continuum manipulator was fixed to the front of the drive unit. The driving wire of the manipulator was guided by the pulley and then connected to the slider. The slider was driven by the nut screw pair, and a tension sensor with a range of 5N was installed between the slider and the nut to measure the tension of the driving wire. A DC servo motor (DCX19S from Maxon Group) was connected to the screw to generate the pulling force. The motor was driven by the digital controller (G-SOLTWI6/100EE01from Elmo Group), and the digital controller was connected to an industrial computer (C6920 from Beckhoff Group) by the EtherCAT bus. The signal of the tension sensor was processed by the transmitter to form a standard voltage signal, and the voltage signal was collected by the industrial computer through the AD converter (EL3164 from Beckhoff Group). The position and posture of the manipulator were measured by the electromagnetic tracking system (Resolution:0.001 mm, VIPER

Table 1

Parameters	Value	Parameters	Value
Thickness of Elastic beam	0.30 mm	Length of rigid joint	2.00 mm
Length of Elastic beam	2.00 mm	Weight mass	0.25 kg
Inner diameter of manipulator	1.00 mm	Initial bending angle of elastic beam	4°
Outer diameter of manipulator	1.75 mm	Initial coordinate of each elastic beam in x_i-axis	1.90 mm
Young modulus	43.00 Gpa	Initial coordinate of each elastic beam in y_i-axis	0.10 mm
Number of elastic beams	7	Friction coefficient	0.2

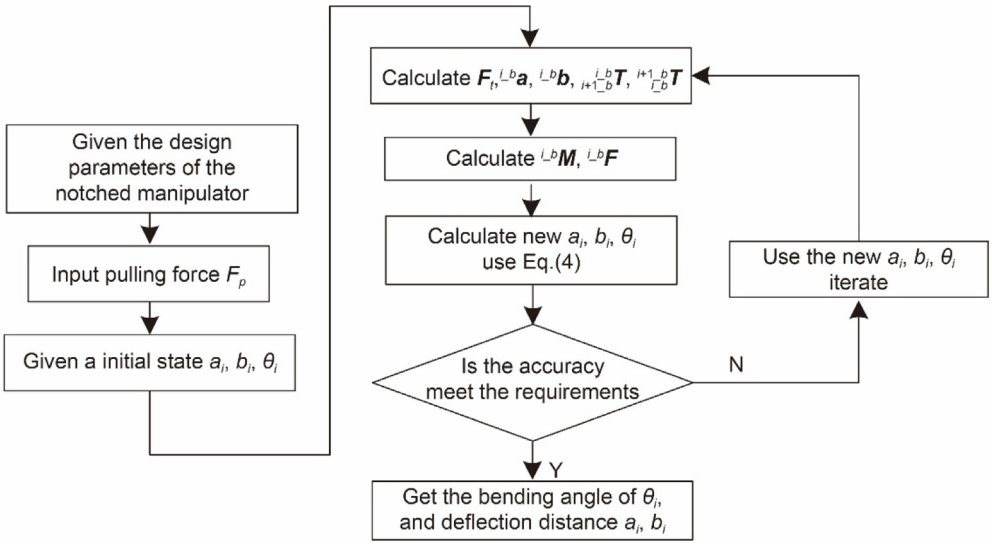

Fig. 7. Iterative calculation process of manipulator bending angle.

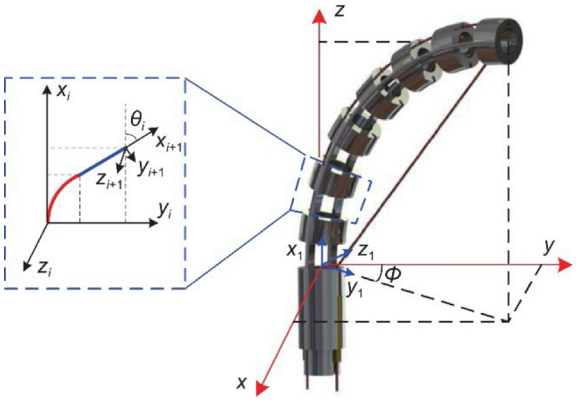

Fig. 8. Kinematics from joint space to Cartesian space.

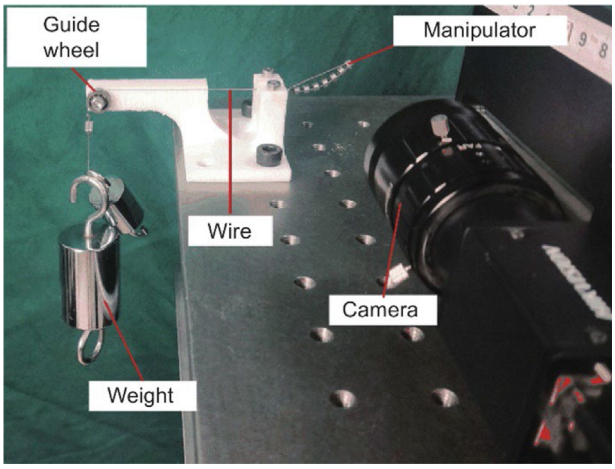

Fig. 9. Experimental setup for the elastic beam bending angle.

4, Polhemus Ltd.). The electromagnetic (EM) sensor (diameter: 0.8 mm) was mounted on the end of the manipulator via a 3D-printed bracket. An EM source was placed in the front of the manipulator to ensure that the sensor was within detection range. PC connected to EM tracking controller via USB for data acquisition. The position and posture of the manipulator were recorded every time the pulling force increased by 50 g until the maximum pulling force reached 350 g. The experimental process was repeated five times, and the average value of the experimental data was taken as the final experimental result.

2.4.1. Manipulator load capacity and stiffness test

To verify the load capacity and stiffness of the manipulator, the performance was verified using the experimental device shown in Fig. 11. The load capacity test of the manipulator needed to simulate a real surgical scene, so a sheath of surgical forceps was passed through the instrument channel. The position of the manipulator without payload was considered as the initial value. As the payload on the manipulator was gradually increased to 400 g, the position of the manipulator was recorded by the EM sensor. The same operation was then repeated with the bending angle of 30°, 45°, 60°, 75°, and 90°, respectively.

3. Results

3.1. Results of elastic beam bending

The experimental results of the elastic beam driven by the 0.25 kg weight are shown in Fig. 12(a). The experimental results

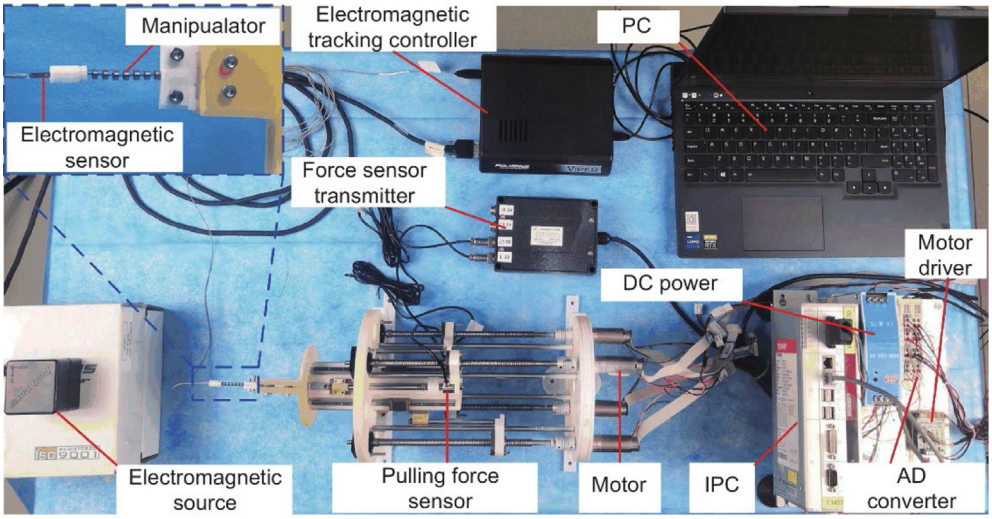

Fig. 10. Manipulator kinematics verification experimental setup.

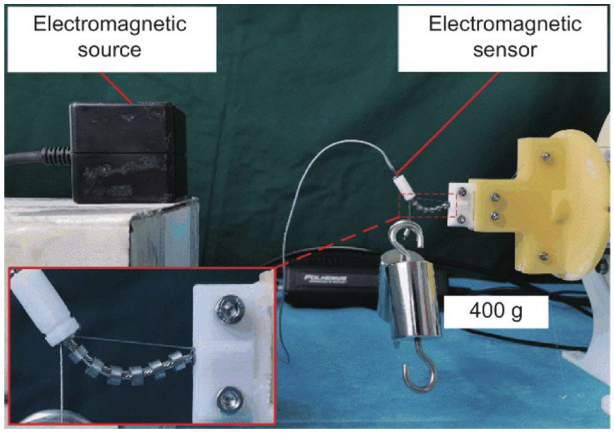

Fig. 11. Experiment setup for manipulator load capacity and stiffness test.

of the elastic beam bending angle have the same distribution as the simulation. The distribution law of the elastic beam bending angle is that the middle is large, and the ends are small. The common assumption that the continuum manipulator has the same bending angle of each elastic beam does not apply to the cable-stayed notch manipulator. The max error of the bending angle occurs at the second elastic beam, about 0.15°. The variance between the experimental results and the simulation results is 0.008°. The smaller variance indicates that the method proposed in this paper can better describe the bending of the elastic beam. The iterative process of the elastic beam bending angle is shown in Fig. 12(b). Although the bending angle fluctuates during the iteration, most angles can reach convergence in the fourth generation. The iterative calculation can be done for all bending angles in the sixth generation. The method proposed in this paper has a faster computing speed.

3.2. Manipulator kinematic model validation

Fig. 13(a) is the experimental result of the bending angle of the manipulator. As the driving force increases, the bending angle and the angle-changing speed of the manipulator gradually increase. This means less tension is required per unit bending angle as the bending angle increases. The maximum error between experimental and simulated values is 3.2°, which is negligible relative to the overall bending of the manipulator. Because the EM tracking sensor is attached to the manipulator through the bracket, the experiment value of the manipulator position includes the length of the bracket, and the length of the bracket is 15 mm. To facilitate the comparison of experimental and simulated values, the length of the bracket is also included in the simulated value.

The experimental results of the manipulator position are shown in Fig. 13(a). The maximum error between the experiment value and simulation value on the y-axis and z-axis is 0.85 mm and 1.52 mm, respectively. Compared to the length of the manipulator, the error rate is less than 5%, which is generally acceptable in engineering applications. The excellent agreement between the experimental value and the simulation value proves the correctness of the kinematics. From Fig. 13(a), it is known that the changing speed of the manipulator bending angle increases with the pulling force. Therefore, in Fig. 13(b), the changing speed of the manipulator position is also gradually increased. Although the experimental and simulated values are in good agreement, there are still errors. The primary sources of errors are the measurement errors of the EM tracking sensor and the manufacturing errors of the manipulator.

3.3. Manipulator load capacity and stiffness test

It can be seen from Fig. 14 that the cable-stayed notch manipulator proposed in this paper shows a good load capacity. When the payload is less than 100 g, the deflection of the manipulator is commonly less than 5 mm. When the payload of the manipulator reaches 400 g, its maximum deflection does not exceed 23 mm. As shown in Fig. 14, the deflection of the manipulator is mainly due to the reverse bending of the elastic beam near the base. The reverse bending of the elastic beam is caused by the combined effect of the payload and the pulling force of the driving wire. As the bending angle of the manipulator gradually increases, the smaller the moment of the payload to the elastic beam near the base, the greater the stiffness of the manipulator. It can be seen from Fig. 14 that the stiffness of the manipulator

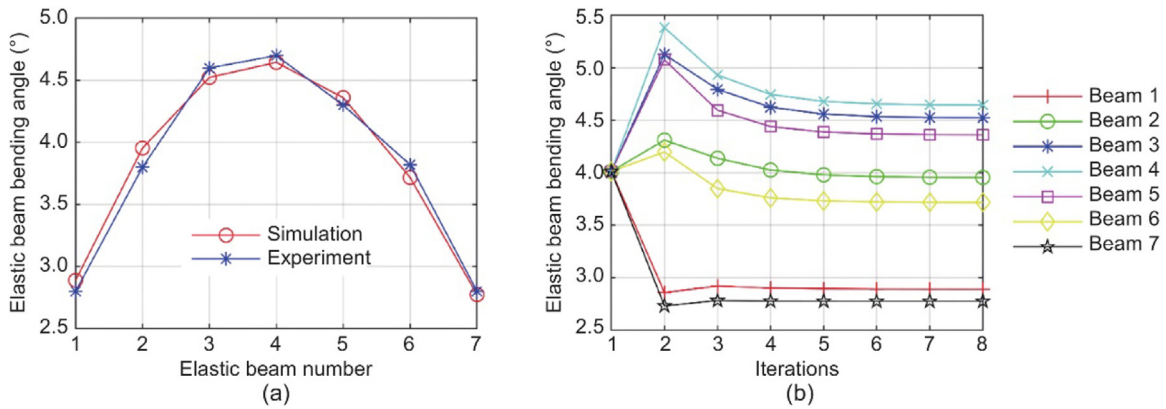

Fig. 12. Results of the elastic beam bending angle. (a) Elastic beam bending angle distribution, (b) Iterations of the elastic beam bending angle.

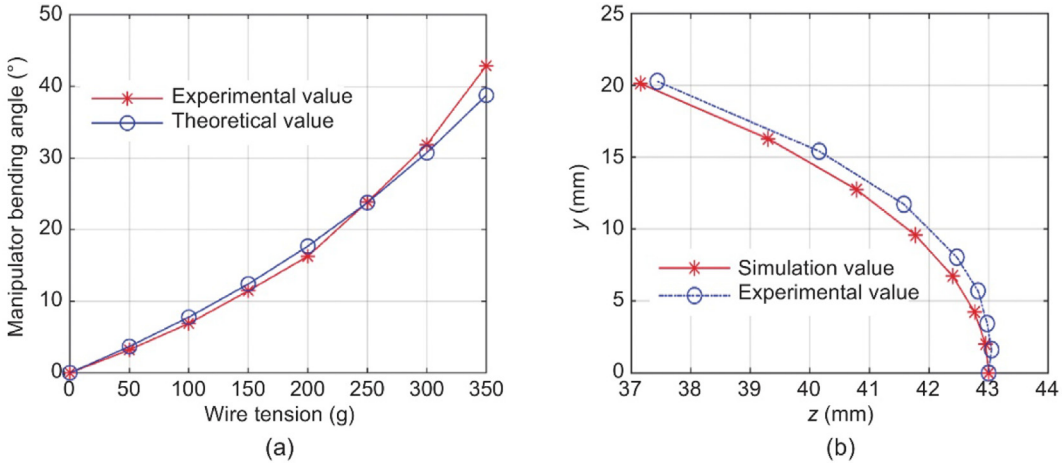

Fig. 13. Position and posture of the manipulator: (a) Theoretical and experimental value of the manipulator bending angle, (b) Theoretical and experimental value of the manipulator position.

gradually increases with the increase of the bending angle. Based on the forces and moments experienced by the elastic beam, the load capacity of the manipulator can be further improved by optimizing the elastic beam stiffness.

4. Conclusions

This paper proposes a cable-stayed notch continuum manipulator for transluminal endoscopic surgery. Since the position and posture of the manipulator are coupled with the pulling force of the driving wire. The bending angle of the elastic beam under the action of force and moment is obtained based on CEIS. The transformation of force and moment between adjacent joints is obtained through coordinate transformation. The bending angle of the elastic beam is obtained by the iterative solution, and then the kinematics from driving space to joint space is obtained. The position and posture of the manipulator are obtained through the bending angle of the elastic beam, and the kinematics from the driving space to the Cartesian space is formed. The elastic beam bending experiment proves that the solution from the drive space to the joint space can be solved by the iterative method proposed in this paper. Manipulator kinematic experiment shows that the kinematics model can accurately describe the motion of the manipulator. The load capacity experiment proves that the cable-stayed notch manipulator has an excellent load capacity. The maximum load of the manipulator can reach 400 g. To the best of our knowledge, the resultant payload was larger than any previously reported payload.

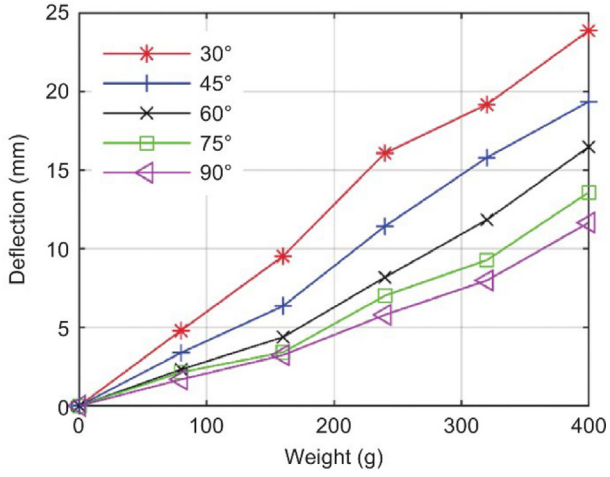

Fig. 14. Deflection of manipulator with different bending angle and payload.

In future work, the structural optimization, inverse kinematics, and variable stiffness of the manipulator will be carried out based on the CEIS.

CRediT authorship contribution statement

Yanqiang Lei: Writing – review & editing, Writing – original draft, Visualization, Supervision, Software, Methodology, Investigation, Funding acquisition, Formal analysis, Data curation, Conceptualization. **Fuxin Du:** Validation, Supervision, Resources. **Huajian Song:** Funding acquisition, Formal analysis. **Liping Zhang:** Resources, Project administration.

Declaration of competing interest

The authors declare that they have no known competing financial interests or personal relationships that could have appeared to influence the work reported in this paper.

Acknowledgments

This work was supported by the National Key Research and Development Program of China (2023YFB4705800 and 2022YFB4 703000), the Key Research and Development Program of Shandong Province, China (2022CXGC010503), and Shandong Provincial Postdoctoral Innovative Talents Funded Scheme, China (238226).

Appendix A. Supplementary data

Supplementary material related to this article can be found online at https://doi.org/10.1016/j.birob.2024.100191.

References

[1] N. Abe, H. Takeuchi, A. Ohki, Y. Hashimoto, T. Mori, M. Sugiyama, Comparison between endoscopic and laparoscopic removal of gastric submucosal tumor, Gastrointest. Endosc. 30 (2018) 7–16.
[2] T.R. McCarty, A.N. Bazarbashi, C.C. Thompson, H. Aihara, Hybrid Endoscopic Submucosal Dissection (ESD) compared with conventional ESD for colorectal lesions: a systematic review and meta-analysis, Endoscopy 53 (10) (2021) 1048–1058.
[3] X. Yang, S. Fu, R. Ji, L. Li, Y. Li, X. Zuo, A novel flexible auxiliary single-arm transluminal endoscopic robot facilitates endoscopic submucosal dissection of gastric lesions (with video), Surg. Endosc. 36 (7) (2022) 5510–5517.
[4] M.T. Chikhaoui, J. Burgner-Kahrs, Control of continuum robots for medical applications: State of the art, ACTUATOR 2018, in: 16th International Conference on New Actuators, VDE, 2018, pp. 1–11.
[5] C. Sun, L. Chen, J. Liu, J.S. Dai, R. Kang, A hybrid continuum robot based on pneumatic muscles with embedded elastic rods, Proc. Inst. Mech. Eng. C 234 (1) (2020) 318–328.
[6] G. Petroni, M. Niccolini, A. Menciassi, P. Dario, A. Cuschieri, A novel intracorporeal assembling robotic system for single-port laparoscopic surgery, Surg. Endosc. 27 (2) (2013) 665–670.
[7] B.P.M. Yeung, T. Gourlay, A technical review of flexible endoscopic multitasking platforms, Int. Surg. J. 10 (7) (2012) 345–354.
[8] K. Xu, J. Zhao, M. Fu, Development of the SJTU Unfoldable Robotic System (SURS) for single port laparoscopy, IEEE/ASME Trans. Mechatron. 20 (5) (2015) 2133–2145.
[9] Y. Kobayashi, Y. Sekiguchi, T. Noguchi, Y. Takahashi, Q. Liu, S. Oguri, K. Toyoda, M. Uemura, S. Ieiri, M. Tomikawa, Development of a robotic system with six-degrees-of-freedom robotic tool manipulators for single-port surgery, Int. J. Med. Robot. Comput. Assist. Surg. 11 (2) (2015) 235–246.
[10] S.J. Phee, S.C. Low, V.A. Huynh, A.P. Kencana, Z.L. Sun, K. Yang, Master and slave transluminal endoscopic robot (MASTER) for natural orifice transluminal endoscopic surgery (NOTES), in: 2009 Annual International Conference of the IEEE Engineering in Medicine and Biology Society, IEEE, United States, 2009, pp. 1192–1195.
[11] K.C. Lau, E.Y.Y. Leung, P.W.Y. Chiu, Y. Yam, J.Y.W. Lau, C.C.Y. Poon, A flexible surgical robotic system for removal of early-stage gastrointestinal cancers by endoscopic submucosal dissection, IEEE Trans. Ind. Inform. 12 (6) (2016) 2365–2374.
[12] J. Wang, S. Wang, J. Li, X. Ren, R.M. Briggs, Development of a novel robotic platform with controllable stiffness manipulation arms for laparoendoscopic single-site surgery (LESS), Int. J. Med. Robot. Comput. Assist. Surg. 14 (1) (2018) e1838.
[13] D.J. Abbott, C. Becke, R.I. Rothstein, W.J. Peine, Design of an endoluminal NOTES robotic system, in: 2007 IEEE/RSJ International Conference on Intelligent Robots and Systems, IEEE, 2007, pp. 410–416.
[14] J. Suh, J. Lee, D. Kwon, Underactuated miniature bending joint composed of serial pulleyless rolling joints, Adv. Robot. 28 (1) (2014) 1–14.
[15] F. Alambeigi, M. Bakhtiarinejad, S. Sefati, R. Hegeman, I. Iordachita, H. Khanuja, M. Armand, On the use of a continuum manipulator and a bendable medical screw for minimally invasive interventions in orthopedic surgery, IEEE Trans. Med. Robot. Bionics. 1 (1) (2019) 14–21.
[16] L. Jiajia, D. Fuxin, L. Yibin, L. Yanqiang, Z. Tao, Z. Gang, A novel inverse kinematics algorithm using the Kepler oval for continuum robots, Appl. Math. Model. 93 (2021) 206–225.
[17] J. Lu, F. Du, F. Yang, T. Zhang, Y. Lei, J. Wang, Kinematic modeling of a class of n-tendon continuum manipulators, Adv. Robot. 34 (19) (2020) 1254–1271.
[18] M. Hwang, D. Kwon, Strong continuum manipulator for flexible endoscopic surgery, IEEE/ASME Trans. Mechatron. 24 (5) (2019) 2193–2203.
[19] Y. Lei, Y. Li, R. Song, F. Du, Development of a novel deployable arm for natural orifice transluminal endoscopic surgery, Int. J. Med. Robot. Comput. Assist. Surg. 17 (3) (2021) e2232.
[20] P.E. Dupont, N. Simaan, H. Choset, C. Rucker, Continuum robots for medical interventions, Proc. IEEE 110 (7) (2022) 847–870.
[21] C. Li, Y. Yan, X. Xiao, X. Gu, H. Gao, X. Duan, X. Zuo, Y. Li, H. Ren, A miniature manipulator with variable stiffness towards minimally invasive transluminal endoscopic surgery, IEEE Robot. Autom. Lett. 6 (3) (2021) 5541–5548.
[22] M.S. Moses, R.J. Murphy, M.D. Kutzer, M. Armand, Modeling cable and guide channel interaction in a high-strength cable-driven continuum manipulator, IEEE/ASME Trans. Mechatron. 20 (6) (2015) 2876–2889.
[23] Z. Du, W. Yang, W. Dong, Kinematics modeling of a notched continuum manipulator, J. Mech. Robot. 7 (4) (2015) 041017.
[24] Z. Du, W. Yang, W. Dong, Kinematics modeling and performance optimization of a kinematic-mechanics coupled continuum manipulator, Mechatronics 31 (2015) 196–204.
[25] G. Zhang, F. Du, S. Xue, H. Cheng, X. Zhang, R. Song, Y. Li, Design and modeling of a bio-inspired compound continuum robot for minimally invasive surgery, Machines 10 (6) (2022) 468.
[26] H. Wang, X. Wang, W. Yang, Z. Du, Z. Yan, Construction of controller model of notch continuum manipulator for laryngeal surgery based on hybrid method, IEEE/ASME Trans. Mechatron. 26 (2) (2021) 1022–1032.
[27] H. Wang, X. Wang, W. Yang, Z. Du, Design and kinematic modeling of a notch continuum manipulator for laryngeal surgery, Int. J. Control Autom. Syst. 18 (11) (2020) 2966–2973.
[28] V. Vitiello, S. Lee, T.P. Cundy, G. Yang, Emerging robotic platforms for minimally invasive surgery, IEEE Rev. Biomed. Eng. 6 (2013) 111–126.
[29] Y. Chen, S.A. Zhang, Z. Wu, B. Yang, Q. Luo, K. Xu, Review of surgical robotic systems for keyhole and endoscopic procedures: state of the art and perspectives, Front. Med. 14 (2020) 382–403.
[30] C. Li, X. Gu, X. Xiao, C.M. Lim, H. Ren, Flexible robot with variable stiffness in transoral surgery, IEEE/ASME Trans. Mechatron. 25 (1) (2019) 1–10.
[31] S. Sefati, R. Hegeman, F. Alambeigi, I. Iordachita, P. Kazanzides, H. Khanuja, R. Taylor, M. Armand, A surgical robotic system for treatment of pelvic osteolysis using an FBG-equipped continuum manipulator and flexible instruments, IEEE/ASME Trans. Mechatron. 26 (1) (2021) 369–380.
[32] Z. Aimei, C. Guimin, A comprehensive elliptic integral solution to the large deflection problems of thin beams in compliant mechanisms, J. Mech. Robot. 5 (2) (2013) 021006.
[33] A. Ehsani-Seresht, S. Hashemi-Pour Moosavi, Dynamic modeling of the cable-driven continuum robots in hybrid position-force actuation mode, Mech. Robot. 12 (5) (2020) 051002.